

# Limits on Light WIMPs with a Germanium Detector at 172 eVee threshold at the China Jinping Underground Laboratory

S.K. Liu,<sup>2,1</sup> Q. Yue,<sup>1,\*</sup> K.J. Kang,<sup>1</sup> J.P. Cheng,<sup>1</sup> H.T. Wong,<sup>7,†</sup> Y.J. Li,<sup>1</sup> S.T. Lin,<sup>2,7</sup> J.P. Chang,<sup>5</sup> N. Chen,<sup>1</sup> Q.H. Chen,<sup>1</sup> Y.H. Chen,<sup>6</sup> Y.C. Chuang,<sup>7,†</sup> Z. Deng,<sup>1</sup> Q. Du,<sup>2</sup> H. Gong,<sup>1</sup> X.Q. Hao,<sup>1</sup> H.J. He,<sup>1</sup> Q.J. He,<sup>1</sup> H.X. Huang,<sup>3</sup> T.R. Huang,<sup>7,†</sup> H. Jiang,<sup>1</sup> H.B. Li,<sup>7,†</sup> J.M. Li,<sup>1</sup> J. Li,<sup>1</sup> J. Li,<sup>5</sup> X. Li,<sup>3</sup> X.Q. Li,<sup>4</sup> X.Y. Li,<sup>4</sup> Y.L. Li,<sup>1</sup> H.Y. Liao,<sup>7,†</sup> F.K. Lin,<sup>7,†</sup> L.C. Lü,<sup>1</sup> H. Ma,<sup>1</sup> S.J. Mao,<sup>5</sup> J.Q. Qin,<sup>1</sup> J. Ren,<sup>3</sup> J. Ren,<sup>1</sup> X.C. Ruan,<sup>3</sup> M.B. Shen,<sup>6</sup> L. Singh,<sup>7,8,†</sup> M.K. Singh,<sup>7,8,†</sup> A.K. Soma,<sup>7,8,†</sup> J. Su,<sup>1</sup> C.J. Tang,<sup>2</sup> C.H. Tseng,<sup>7,†</sup> J.M. Wang,<sup>6</sup> L. Wang,<sup>1,2</sup> Q. Wang,<sup>1</sup> S.Y. Wu,<sup>6</sup> Y.C. Wu,<sup>1</sup> Y.C. Wu,<sup>5</sup> Z.Z. Xianyu,<sup>1</sup> R.Q. Xiao,<sup>1</sup> H.Y. Xing,<sup>2</sup> F.Z. Xu,<sup>1</sup> Y. Xu,<sup>4</sup> X.J. Xu,<sup>1</sup> T. Xue,<sup>1</sup> C.W. Yang,<sup>2</sup> L.T. Yang,<sup>1</sup> S.W. Yang,<sup>7,†</sup> N. Yi,<sup>1</sup> C.X. Yu,<sup>4</sup> H. Yu,<sup>1</sup> X.Z. Yu,<sup>2</sup> X.H. Zeng,<sup>6</sup> Z. Zeng,<sup>1</sup> L. Zhang,<sup>5</sup> Y.H. Zhang,<sup>6</sup> M.G. Zhao,<sup>4</sup> W. Zhao,<sup>1</sup> Z.Y. Zhou,<sup>3</sup> J.J. Zhu,<sup>2</sup> W.B. Zhu,<sup>5</sup> X.Z. Zhu,<sup>1</sup> and Z.H. Zhu<sup>6</sup>

(CDEX Collaboration)

<sup>1</sup>Key Laboratory of Particle and Radiation Imaging (Ministry of Education) and Department of Engineering Physics, Tsinghua University, Beijing 100084

<sup>2</sup>School of Physical Science and Technology, Sichuan University, Chengdu 610065

<sup>3</sup>Department of Nuclear Physics, China Institute of Atomic Energy, Beijing 102413

<sup>4</sup>School of Physics, Nankai University, Tianjin 300071

<sup>5</sup>NUCTECH Company, Beijing 10084

<sup>6</sup>YaLong River Hydropower Development Company, Chengdu 610051

<sup>7</sup>Institute of Physics, Academia Sinica, Taipei 11529

<sup>8</sup>Department of Physics, Banaras Hindu University, Varanasi 221005

(Dated: September 15, 2022)

The China Dark Matter Experiment reports results on light WIMP dark matter searches at the China Jinping Underground Laboratory with a germanium detector array with a total mass of 20 g. The physics threshold achieved is 172 eVee at 50% signal efficiency. With 0.784 kg-days of data, exclusion region on spin-independent coupling with the nucleon is derived, improving over our earlier bounds at WIMP mass less than 4.6 GeV.

PACS numbers: 95.35.+d, 98.70.Vc, 29.40.Wk

## I. INTRODUCTION

Compelling evidence from astroparticle physics and cosmology indicates that dark matter constitutes about 27% of the energy density of our Universe [1]. Weakly Interacting Massive Particles (WIMPs, denoted by  $\chi$ ) are the leading candidate for Cold Dark Matter (CDM) [2]. It is expected that WIMPs would interact with normal matter through elastic scattering. Direct detection of WIMPs has been attempted with different detector technologies [3]. The anomalous excess of unidentified events at low energy with the DAMA [4], CoGeNT [5], CRESST-II [6] and CDMS (Si) [7] data has been interpreted as signatures of light WIMPs. They are however inconsistent with the null results from XENON [8, 9], TEXONO [10], CDMSlite [11] and LUX [12] experiments. It is crucial to continue probing WIMPs with lower mass achievable by available techniques.

Our earlier measurements [13] have provided the first results on low-mass WIMPs from the China Dark Matter Experiment phase I (CDEX-1). With a 994 g point-contact germanium detector, an energy threshold of 400 eVee (“ee” represents electron equivalent energy) was

achieved. The experiment was performed at the China Jinping Underground Laboratory (CJPL) [14], which was inaugurated at the end of 2010. With a rock overburden of more than 2400 m giving rise to a measured muon flux of  $61.7 \text{ y}^{-1} \cdot \text{m}^{-2}$  [15], CJPL provides an ideal location for low-background experiments.

We report final results of the “CDEX-0” experiment at CJPL, which is based on a pilot measurement with an existing prototype Ge detector with sub-keV energy threshold at a few gram modular mass. The experimental set-up, candidate event selection procedures and constraints on WIMP-nucleon spin-independent elastic scattering are discussed in the subsequent sections.

## II. EXPERIMENTAL SET-UP

The CDEX-0 detector was previously used by the TEXONO experiment at a surface laboratory, where constraints on light-WIMP were placed with a data set having a threshold of 220 eVee at 50% signal efficiency [16]. The schematic design is depicted in Fig. 1. The NaI(Tl) crystal scintillator whose threshold is about 10 keVee served as an anti-Compton (AC) detector which enclosed the cryostat. The thickness of its side is 48 mm and top is 130 mm. The passive shielding system includes, from outside to inside, 1 m of polyethylene, 20 cm of lead, 20

\* Corresponding author: yueq@mail.tsinghua.edu.cn

† Participating as a member of TEXONO Collaboration

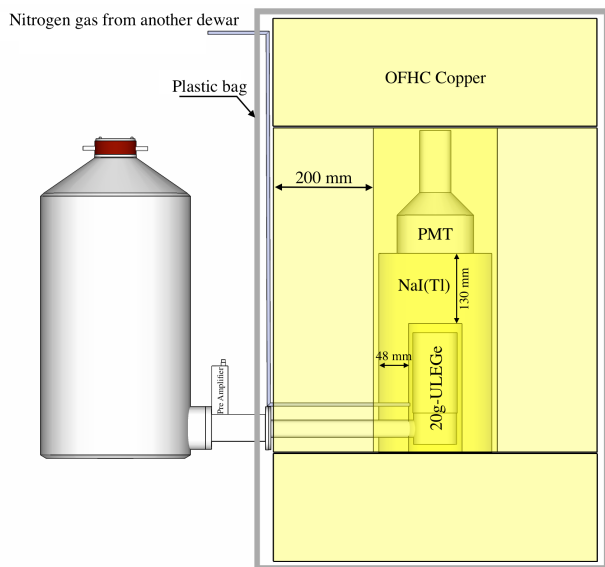


FIG. 1. Schematic diagram of the experimental set-up which includes the germanium detector array and NaI(Tl) anti-Compton detector, as well as the enclosing OFHC Cu shielding. The entire structure is placed inside a passive shielding system described in Ref.[14].

cm of borated polyethylene and 20 cm of OFHC (Oxygen-Free High-Conductivity) copper. A plastic bag enclosing the OFHC copper was purged by nitrogen gas evaporated from the liquid nitrogen dewar. The detailed information about the passive shielding system was described in reference [14].

The 20 g germanium detector consists of four n-type crystals. Every crystal with an active mass of 5 g has a semi-planar configuration with a  $p^+$  electrode on the outer surface, and a  $n^+$  contact of a small diameter is used as the central electrode, from which signals are derived. The surface electrode is of  $\mu\text{m}$  thickness fabricated by boron-ion implantation. The crystal array is encapsulated within the cryostat made of OFHC copper and the crystal center-to-center spacing is 14 mm. The cryostat end cap is made of carbon composite with the thickness of 0.6 mm allowing calibration with low-energy X-rays outside.

The schematic diagram of the electronics and data acquisition (DAQ) system is shown in Fig. 2. The  $n^+$  contact signal is read out by low noise FET in the vicinity of the Ge-crystal and fed into a reset preamplifier. Each crystal has its respective preamplifier and two identical outputs distributed to two shaping amplifiers at 6  $\mu\text{s}$  ( $SA_6$ ) and 12  $\mu\text{s}$  ( $SA_{12}$ ) shaping time. One output from  $SA_6$  was fed into the discriminator to supply the trigger for DAQ system. The signals were sampled and recorded by a 100 MHz flash analog-to-digital converters (FADC). The recording time intervals were 70  $\mu\text{s}$  and 110  $\mu\text{s}$  for the signals at  $SA_6$  and  $SA_{12}$ , respectively. The PMT outputs from the AC detector at two different gain factors were also digitized. Events provided by a random

trigger (RT) with a pulse generator at 0.05 Hz were also recorded for calibration and efficiencies measurement. A veto period of 4 ms is applied after every preamplifier set to reject electronic-induced noise [13].

The relative timing of the Ge and AC detectors were recorded by standard Time to Digital Converters (TDC) with 25 ps resolution and a full range of 52  $\mu\text{s}$ . In addition, the extended trigger time tag (ETTT) TDC extended the dynamic range to a full scale range up to 100 seconds maintaining the 25 ps resolution. It is used to detect long-duration temporal correlations, such as those between the Ge and the reset signal.

At a total DAQ rate of 6.9 Hz, the DAQ live time was measured to be 89.9 % by RT-events. The anomalously large dead time was due to inefficient methods of hardware synchronization in the prototype DAQ system, which were fixed in our subsequent data taking. The optimal area from  $SA_6$  was chosen as the energy measurements. Energy calibration was achieved by the external X-ray peaks from Ca, Mn, Ti, Cu which were produced by the X-ray generator illuminating a mixture of these elements, as displayed in Fig. 3 [17].

The zero-energy was defined by the random trigger events. The calibration uncertainties are 0.52 eVee and 0.53 eVee at 100 eVee and 1 keVee, respectively. The measured parameters which characterize the resolution of the four crystals are shown in Table I. Crystal #2 provided the best performance and was adopted for subsequent analysis. The data acquisition live time is 0.784 kg-days, corresponding to 174-days of data taking. Inclusion of data from the other crystals to the analysis would not provide substantial improvement to the final physics results.

TABLE I. Measured parameters which characterize the resolution performance of the four crystals.

Crystal no.	Pedestal RMS (eVee)	Noise Edge (eVee)	FMHM of Ca X-rays at 3.69 keV (eVee)	Trigger Eff. at 50% (eVee)
1	51.3	$\sim 300$	$168.7 \pm 2.6$	$171.0 \pm_{4.5}^{3.7}$
2	32.6	$\sim 180$	$123.4 \pm 3.1$	$96.8 \pm_{1.5}^{1.3}$
3	64.4	$\sim 400$	$186.0 \pm 6.1$	$267.0 \pm_{2.5}^{2.1}$
4	67.8	$\sim 250$	$182.0 \pm 5.9$	$146.0 \pm_{3.5}^{2.7}$

Events in Ge-crystal in coincidence (anti-coincidence) with the AC detector are denoted as  $AC^{+(-)}$ , respectively. Physics events induced by  $\gamma$ -rays are selected by the  $AC^+$  tag and are used to optimize the selection criteria and to evaluate the signal efficiencies. Two complementary data set were adopted. A  $^{60}\text{Co}$  source placed external to the NaI-AC detector provided high statistics data giving accurate measurement of the efficiencies, while the in situ low-background  $AC^+$  data served as consistency cross-check.

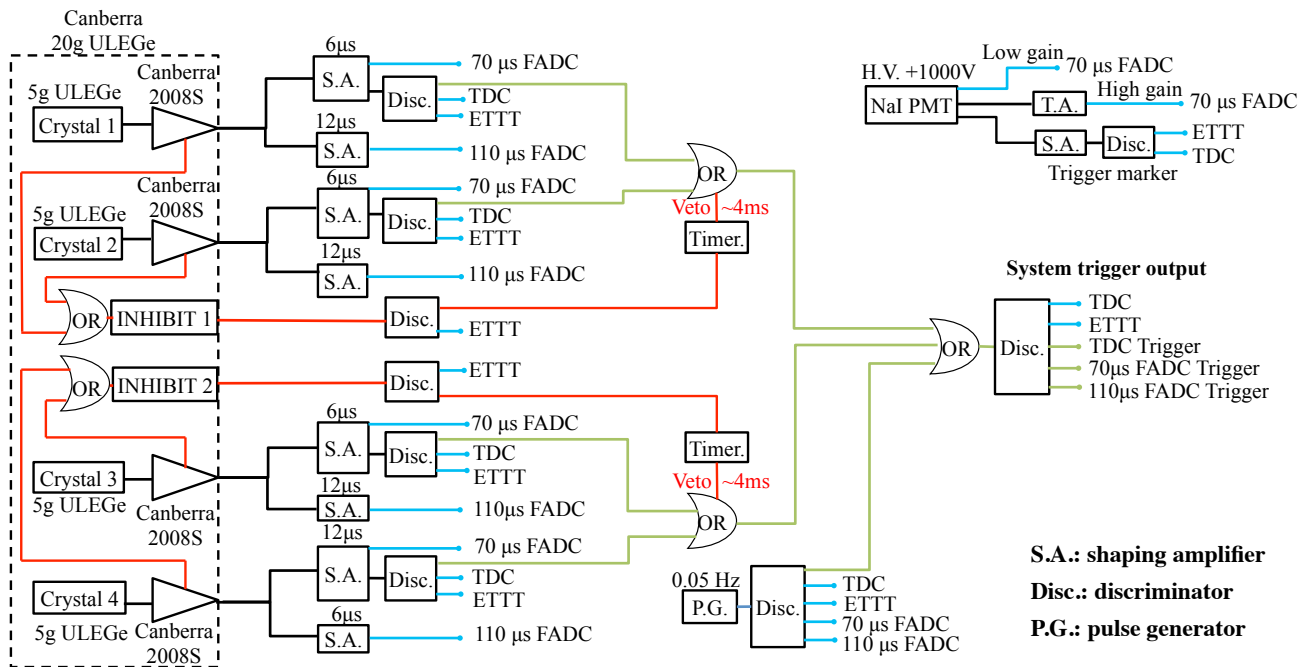


FIG. 2. Schematic diagram of the electronics and DAQ system of the germanium array and the NaI(Tl) detector.

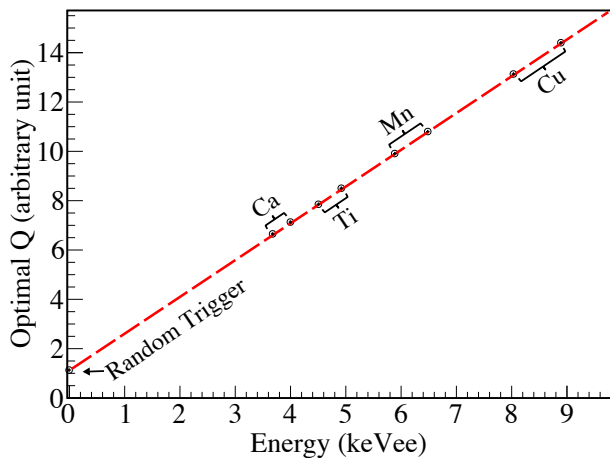


FIG. 3. Calibration line relating the optimal Q measurements from SA<sub>6</sub> with the known energies from X-ray sources. The error bars are smaller than the data point size.

### III. CANDIDATE EVENT SELECTION

WIMP-induced interactions are characterized by being single-site events uncorrelated with other detector components, and having the same pulse shape as the events due to genuine physical processes. A series of data analysis criteria were adopted to select the  $\chi$ N events, and their corresponding signal efficiencies were measured. The details are discussed as follows, while the results are summarized in Table II.

1. Timing (TM) Selection: the preamplifier RESET induces noise events with definite timing structure. The timing profiles of the RESET and the events are illustrated in Fig. 4 (a). The timing distribution between an event and its previous RESET, denoted by  $T_-$ , is depicted in Fig. 4 (b) for physics events and RT. A cut of  $T_- < 0.1$  ms removes all RESET-induced background. The RESET period ( $\Delta T$ ) distribution is shown in Fig. 4 (c). The duration in which at least five consecutive periods persistently below 0.7 s is rejected. They correspond to temporary surge of leakage currents in the detector. The signal efficiency is derived from the survival probability of the RT events, and was measured to be 91.13%.

2. Anti-Compton ( $AC^-$ ) Selection: the time difference between the AC and the Ge-trigger instant is depicted in Fig. 5. The band corresponds to  $AC^+$  events with coincidence of the Ge and NaI. The dependence with energy is due to the slow shaping pulse taking longer time at lower energy to cross a fixed threshold in the discriminator. The signal efficiency is 99.9% from the survival probability of the RT events.

3. Physics versus electronic noise (PN) Selection: these events can be differentiated by their pulse shape parameters as defined in Fig. 6. The energy-independent  $PN_i$  selection is based on the pedestal (Ped) stability, as illustrated in Fig. 7, while the energy-dependent  $PN_d$  cuts make use of the minima (MIN) and maxima (MAX) of the pulse, the location of the maxima ( $t_{MAX}$ ) and the pulse width (PW), as depicted in Fig. 8.

Signal efficiencies of  $PN_i$  are derived by the survival of the RT events to be 98.9%, while those for  $PN_d$  are

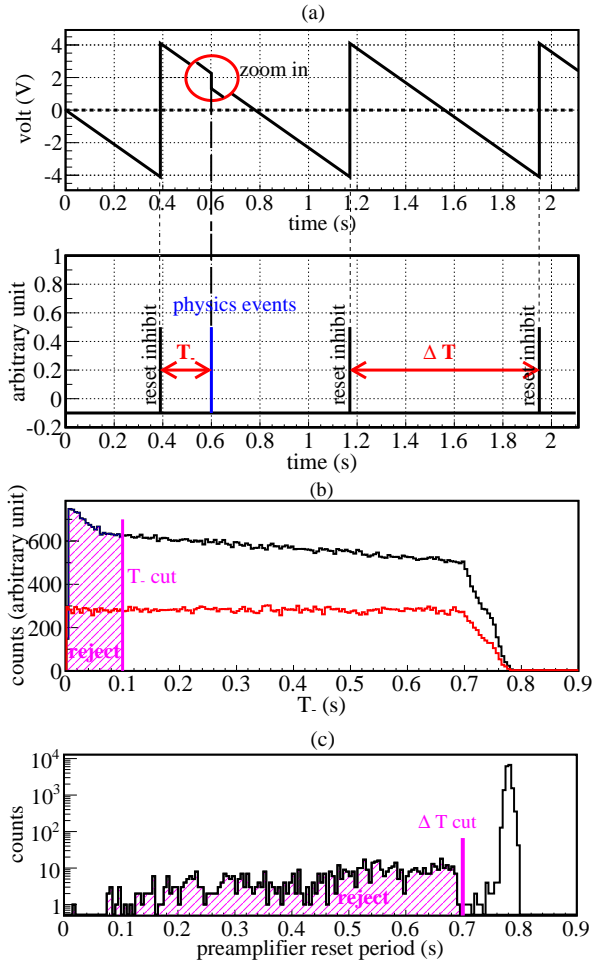


FIG. 4. (a) Raw signal from the reset preamplifier along with the timing of reset-inhibit and a typical physics event. (b) The distributions of  $T$  for random trigger events (red) and background events (black) are shown as well as the rejected parameter space. (c) The reset period cut and its rejected parameter space are displayed.

from the survival of  $AC^+$  events from  $^{60}\text{Co}$  source and in situ background. They are displayed as red crosses and compared with the  $AC^-$  background distributions in the selection plots of Fig. 8 (a)-(d). The combined efficiencies of all cuts (including TM,  $AC^-$ ,  $PN_i$  and  $PN_d$ ) are shown in Fig. 9. The trigger efficiency, also shown in Fig. 9, is evaluated from the survival probabilities of precision pulser and in situ physics events via an extrapolation of the amplitude distributions to sub-noise edge energy. As shown in Fig. 9, the physics threshold is  $172 \pm 4$  eVee at 50% combined analysis efficiency. The signal efficiencies and background suppression factors at threshold and at a high energy bin are summarized in Table II to illustrate and compare the effects of each process.

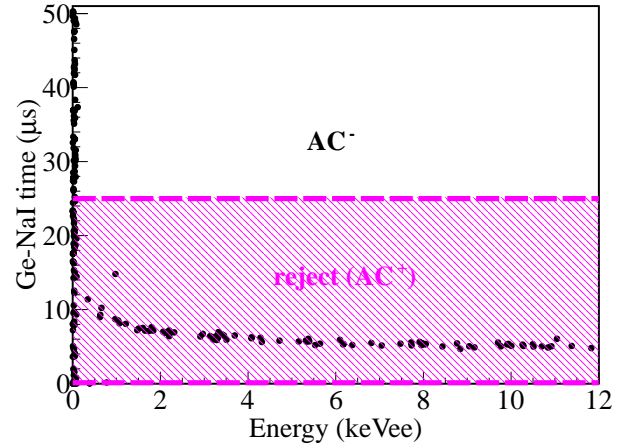


FIG. 5. Scatter plots of the difference between Ge and NaI(Tl) timing versus measured energy along with  $AC^-$  selection and rejected parameter space.

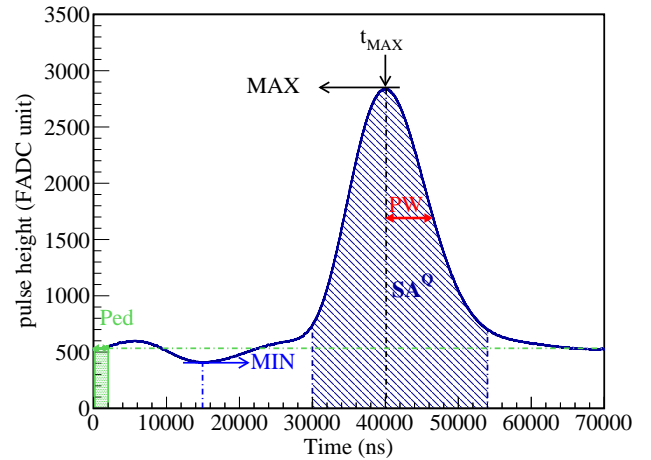


FIG. 6. Pulse shape parameters for PN-Selection: Ped is the average of the first 200 time bins; MIN and MAX are the minima and maxima of the pulses, respectively,  $t_{MAX}$  is the location of the maxima relative to the trigger instant and PW characterizes the pulse width. Energy is defined by the area  $SA_6^Q$ .

#### IV. CONSTRAINS ON LIGHT WIMPS

The measured raw spectra and those at different stages of the analysis are depicted in Fig. 10. The only explicit structure observed was the 8.041 keV Copper  $K\alpha$  X-ray. The spectrum of events that survived all selection criteria is flat above 1.5 keVee, due to ambient radioactivity of high energy  $\gamma$ -rays. The residual spectrum after subtraction of this background channel is depicted in the inset of Fig. 10.

The energy spectra due to  $\chi N$  spin-independent interactions cannot be larger than the residual spectrum. The

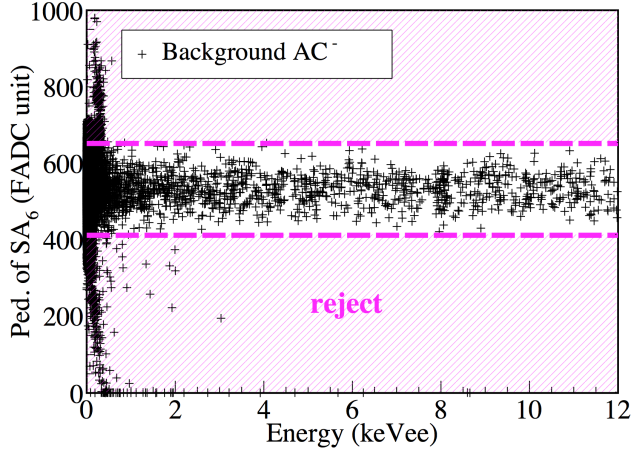


FIG. 7. Energy-independent  $PN_i$  cut on Ped of  $SA_6$ .

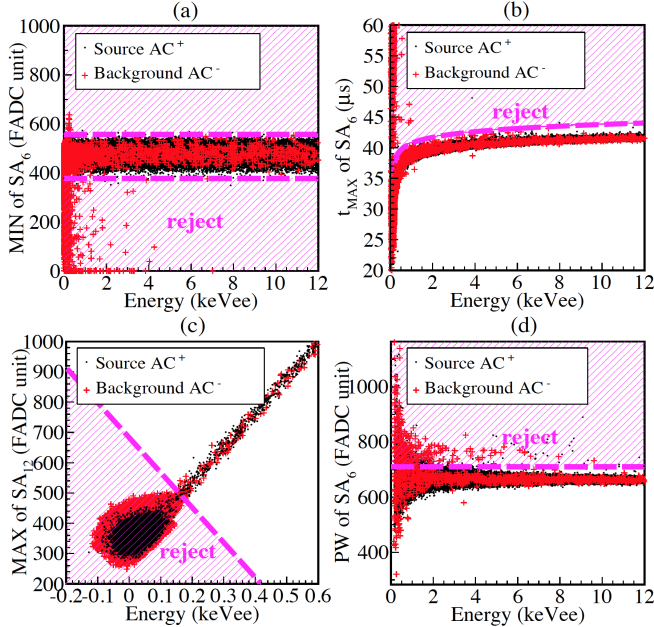


FIG. 8. The energy-dependent  $PN_d$  cuts, based on the parameters defined in Fig. 6.

thickness of the surface inactive layer [18] is only tens of micrometers and can be neglected. Upper limits on their cross-sections ( $\sigma_{\chi N}^{SI}$ ) as a function of WIMP-mass are derived, using the binned Poisson method [19]. The input parameters include quenching factor given by the TRIM program [20], standard WIMP halo assumption [21], conventional astrophysical models (local WIMP density of  $0.3 \text{ GeV} \cdot \text{cm}^{-3}$  and Maxwellian velocity distribution with  $\nu_0 = 220 \text{ km} \cdot \text{s}^{-1}$ , the escape velocity  $\nu_{\text{esc}} = 544 \text{ km} \cdot \text{s}^{-1}$ ) and energy resolution of detector derived from the calibration data.

The exclusion curve at 90% confidence level is shown in Fig. 11, together with those of several selected ex-

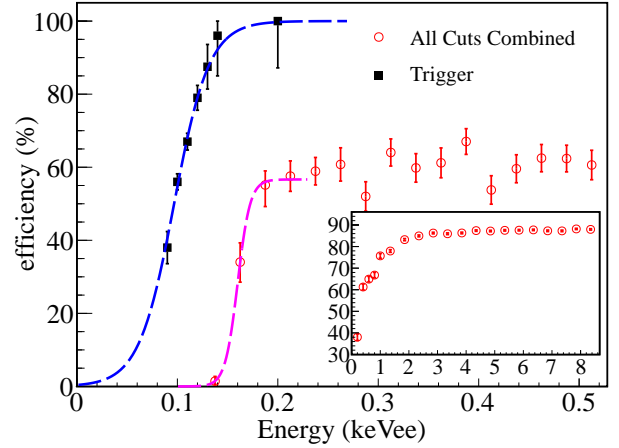


FIG. 9. The trigger efficiencies and those of all selection procedures combined. The combined efficiencies in an extended energy range are depicted in the inset, in which the error bars are smaller than the data point size.

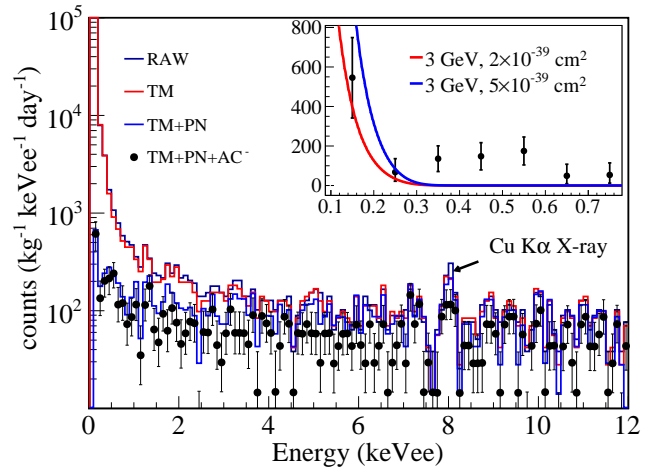


FIG. 10. Measured energy spectra of 20g-ULEGe, showing the raw spectra and those at the different stages of the analysis. The inset figure shows the low energy spectrum after subtraction of a flat background due to high-energy  $\gamma$ -rays, superimposed with the predicted spectra for 3 GeV WIMPs with  $\sigma_{\chi N}^{SI} = 2 \times 10^{-39} \text{ cm}^2$  and  $\sigma_{\chi N}^{SI} = 5 \times 10^{-39} \text{ cm}^2$ .

periments [4–13, 16, 22]. The previous results of CRESST-I [22] and TEXONO [16] are re-analyzed using the currently-favored astrophysical parameters. Under this consistent analysis, this result improves over our earlier bounds at WIMP mass range of  $1.3 \text{ GeV} < M_\chi < 4.6 \text{ GeV}$ , and over the published limit [11] at  $M_\chi < 3.5 \text{ GeV}$ . The predicted  $\chi N$  recoil spectra due to the allowed (excluded)  $\sigma_{\chi N}^{SI}$  at  $m_\chi = 3 \text{ GeV}$  are superimposed with the residual spectrum in the inset of Fig. 10.

TABLE II. Summary of candidate event selection procedures at two representative energy intervals. Listed are the individual and cumulative background survival fraction [ $\lambda$ (%) and  $\Pi\lambda$ (%), respectively] and the candidate signal efficiency [ $\epsilon$ (%)], as well as “Combined Efficiency” multiplying all efficiency factors together including trigger efficiency, TM,  $\text{PN}_i$ ,  $\text{PN}_d$  and  $\text{AC}^-$  efficiencies.

Energy bin	100-200 eVee	600-700 eVee
Raw background counts	122900	84
DAQ dead time (%)	10.05±0.03	
Trigger efficiency (%)	89.51±1.2	100
Timing Selection:		
$\lambda[\Pi\lambda]$ (%)	96.34 [96.34]	79.03 [79.03]
$\epsilon$ (%)	91.13±0.03	
$\text{PN}_i$ cuts:		
$\lambda[\Pi\lambda]$ (%)	97.27 [93.70]	73.47 [58.06]
$\epsilon$ (%)	98.87±0.01	
$\text{PN}_d$ cuts:		
$\lambda[\Pi\lambda]$ (%)	0.01 [0.01]	27.78 [16.13]
$\epsilon$ (%)	25.83± $^{2.23}_{2.40}$	73.58±1.95
Anti-Compton Selection:		
$\lambda[\Pi\lambda]$ (%)	90.9 [0.01]	60.00 [9.68]
$\epsilon$ (%)	99.99±0.01	
Combined Efficiency(%)	20.82± $^{2.03}_{2.18}$	66.30±1.76
After-all-cuts counts	10	6
After-all-cuts rate ( $\text{kg}^{-1}\text{keV}^{-1}\text{day}^{-1}$ )	612± $^{204}_{203}$	115± $^{58}_{39}$

## V. SUMMARY AND PROSPECTS

The results presented in this article correspond to the first completed program of the pilot experiment at the new underground facility CJPL. Improved constraints are derived with a conventional Ge detector of good threshold response but only a few gram modular target mass. Novel p-type point-contact germanium detectors were developed in the past few years [23], offering sub-keV energy threshold with kg-scale target such that the background level per unit mass is greatly reduced due to self-attenuation effects. Dark matter experiments with

this detector technique are being pursued at CJPL [13] and elsewhere [5, 10, 16]. The projected sensitivities of the realistic benchmark sensitivities of 100 eVee threshold at  $1 \text{ kg}^{-1} \text{ keV}^{-1} \text{ day}^{-1}$  background level for 10 kg-year exposure is overlaid in Fig. 11.

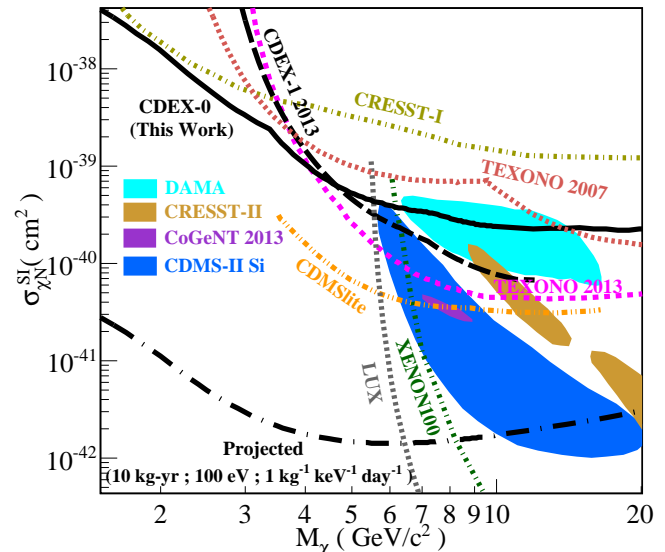


FIG. 11. Exclusion plot of spin-independent  $\chi_N$  coupling at 90% confidence level, superimposed with the results from other benchmark experiments. Allowed regions given by CoGeNT [5], DAMA/LIBRA [4], CDMS-II (Si) [7] and CRESST-II [6] are presented, as well as the exclusion limits from XENON100 [9], CDMSlite [11], LUX [12], CDEX-1 (2013) [13], TEXONO [10, 16], and CRESST-I [22]. The potential reach at indicated projected sensitivities with point-contact germanium detectors is also displayed.

## ACKNOWLEDGMENTS

This work was supported by the National Natural Science Foundation of China (Contracts No.10935005, No. 10945002, No. 11275107 and No. 11175099) and National Basic Research program of China (973 Program) (Contract No. 2010CB833006) and NSC 99-2112-M-001-017-MY3 and Academia Sinica Principle Investigator Award 2011-2015 from Taiwan.

[1] J. Beringer *et al.*, Phys. Rev. D **86**, 010001 (2012), and references therein; P. A. R. Ade *et al.*, (2013), arXiv:1303.5076.  
[2] C. Kelso, D. Hooper, and M. R. Buckley, Phys. Rev. D **85**, 043515 (2012), and references therein.  
[3] J. D. Lewin and P. F. Smith, Astropart. Phys. **6**, 87 (1996).  
[4] P. Belli *et al.*, Phys. Rev. D **84**, 055014 (2011); R. Bernabei *et al.*, Eur. Phys. J. C **67**, 39 (2010).  
[5] C. E. Aalseth *et al.*, Phys. Rev. Lett. **106**, 131301 (2011); Phys. Rev. D **88**, 012002 (2013); arXiv:1401.3295v1.

[6] G. Angloher *et al.*, Eur. Phys. J. C **72**, 1971 (2012).  
[7] R. Agnese *et al.*, Phys. Rev. Lett. **111**, 251301 (2013).  
[8] J. Angle, Phys. Rev. Lett. **110**, 249901 (2013).  
[9] E. Aprile *et al.*, Phys. Rev. Lett. **109**, 181301 (2012).  
[10] H. B. Li *et al.*, Phys. Rev. Lett. **110**, 261301 (2013); Astropart. Phys. **56**, 1 (2014).  
[11] R. Agnese *et al.*, Phys. Rev. Lett. **112**, 041302 (2014).  
[12] D. S. Akerib *et al.*, (2013), arXiv:1310.8214.  
[13] W. Zhao *et al.*, Phys. Rev. D **88**, 052004 (2013); K. J. Kang *et al.*, Chinese Phys. C **37**, 126002 (2013).  
[14] K. J. Kang *et al.*, Front. Phys. **8**, 412 (2013).

- [15] Y. C. Wu *et al.*, Chinese Phys. C **37**, 086001 (2013).
- [16] S. T. Lin *et al.*, Phys. Rev. D **79**, 061101 (2009).
- [17] Y. C. Wu *et al.*, J Tsinghua Univ (Sci & Technol) **53**, 1365 (2013).
- [18] U. Tamm, W. Michaelis, and P. Coussieu, Nucl. Instrum. Methods **48**, 301 (1967); M. G. Strauss and R. N. Larsen, **56**, 80 (1967); E. Sakai, IEEE Trans. Nucl. Sci. **18**, 208 (1971).
- [19] C. Savage, G. Gelmini, P. Gondolo, and K. Freese, J. Cosmol. Astropart. Phys. **2009**, 010 (2009).
- [20] J. F. Ziegler, Nucl. Instrum. Methods Phys. Res., Sect. B **219-220**, 1027 (2004); S. T. Lin *et al.*, arXiv:0712.1645v4.
- [21] F. Donato, N. Fornengo, and S. Scopel, Astropart. Phys. **9**, 247 (1998).
- [22] G. Angloher *et al.*, Astropart. Phys. **18**, 43 (2002).
- [23] P. N. Luke, F. S. Goulding, N. W. Madden, and R. H. Pehl, IEEE Trans. Nucl. Sci. **36**, 926 (1989); P. S. Barbeau, J. I. Collar, and O. Tench, J. Cosmol. Astropart. Phys. **2007**, 009 (2007).